JACS
JOURNAL OF THE AMERICAN CHEMICAL SOCIETY
pubs.acs.org/JACS
Article

Ultrafast Joule-Heating Disproportionation for Engineering Sub-2 nm Si Nanodomains toward Stable, High-Performance SiO Anodes

Jiarui Li, Quan Nie, Te Kang, Ge Qu, Fangzhou Yang, Wang Wan, Long Yang, Chao Wang,* and Yunhui Huang*

Cite This: J. Am. Chem. Soc. 2026, 148, 26017−26026
Read Online
ACCESS | Metrics & More | Article Recommendations | Supporting Information

ABSTRACT: Silicon monoxide (SiO) is a promising anode material for lithium-ion batteries but suffers from significant volume expansion and poor cycling stability. We demonstrate that SiO undergoes electrochemical disproportionation during cycling, forming Si nanodomains that stabilize the structure. Traditional thermal disproportionation methods struggle with controllability and are energy-intensive. Here, we introduce flash joule heating (FJH) for prestabilization, achieving disproportionation in 0.3 s with significantly improved energy efficiency. The ultrafast heating enables better control over size, density, and crystallinity of Si nanodomains while preventing SiO_2 crystallization. The resulting ∼1.5 nm Si nanodomains, embedded in an amorphous SiO_2 matrix, enhance electrochemical performance and reduce volume expansion. The optimized anodes deliver a specific capacity of 1419 mAh g^{-1} with 96.6% retention after 150 cycles and 88.6% retention after 300 cycles in NCM811 full cells. This work establishes FJH as an efficient method for pre-engineering SiO, offering a promising route to durable, high-performance anodes.

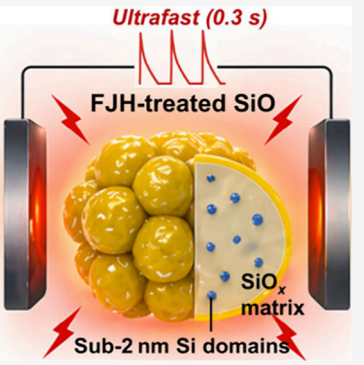

INTRODUCTION

Silicon (Si) is considered one of the most promising anode materials for lithium-ion batteries (LIBs) due to its high theoretical capacity (3579 mAh g^{-1}, nearly 10 times that of graphite), low lithiation potential (<0.5 V), and natural abundance.[1,2] However, its practical application is hindered by significant volumetric expansion (≥300%) during lithiation,[3−5] which induces mechanical stress, causing particle cracking, electrical disconnection, and the breakdown of the solid electrolyte interphase (SEI), leading to rapid capacity degradation and poor cyclability. In contrast, silicon monoxide (SiO),[6,7] a Si derivative with a theoretical capacity of ∼2680 mAh g^{-1}, has emerged as a promising alternative.[8,9] Unlike Si, which undergoes alloying with Li, SiO experiences a solid-solution-like reaction, resulting in lower volume expansion.[10,11] This provides a favorable balance between capacity and cycling stability, making SiO a viable option for improving both capacity retention and long-term performance.[11] However, SiO still faces challenges such as large initial irreversible capacity, poor intrinsic conductivity, and residual volume expansion, limiting its practical application.[9]

To address these challenges, various strategies have been explored, including ball milling,[12−14] carbon coating,[15−19] porosity modulation,[20] and thermal disproportionation.[21−25] Among these, thermal disproportionation has received particular attention. The mechanism is shown in eq 1:

$$2SiO \rightarrow Si + SiO_2 \quad (1)$$

This process generates Si and SiO_2, with Si forming nanometer-sized particles that enhance electrochemical activity and stability, while the SiO_2 matrix provides mechanical buffering.[26,27] Sohn et al. employed tube furnace heating at temperatures between 800 and 1200 °C under an Ar atmosphere for 3 h, increasing the Si particle size from ∼5 nm to ∼30 nm, along with improved crystallinity. High-energy ball milling was then used to disrupt the well-crystallized SiO_2 shell, exposing active Si nanodomains and significantly improving reversible capacity and cycling stability.[25] Li et al. observed that higher treatment temperatures produced larger Si nanodomains but resulted in poorer cycling performance. To prevent over disproportionation, they optimized the process by treating the material at 450 °C for 2 h, resulting in 4−6 nm Si nanodomains with low crystallinity, achieving the best balance between capacity and stability.[23]

Interestingly, we discovered that SiO undergoes slow and random electrochemical disproportionation during cycling, gradually forming Si nanodomains that help stabilize the electrode. Based on previous findings, we conclude that the following conditions should be targeted to optimize the performance of SiO disproportionation:

Received: March 5, 2026
Revised: May 28, 2026
Accepted: June 1, 2026
Published: June 15, 2026

https://doi.org/10.1021/jacs.6c04827
J. Am. Chem. Soc. 2026, 148, 26017−26026

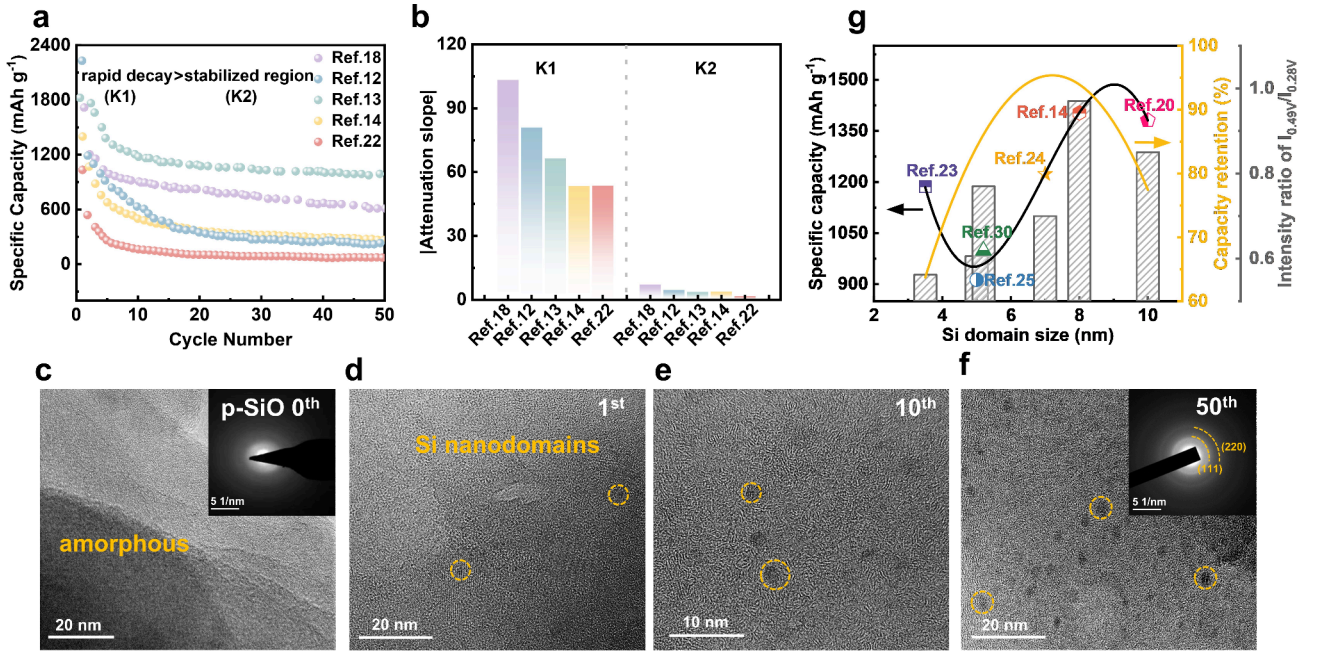

Figure 1. Electrochemical disproportionation-induced nanostructure evolution of pristine SiO. a) The literature reported two-stage capacity decay behavior of p-SiO. b) Extracted fading rates (K1, K2) from meta-analysis of prior reports. c) TEM image of fresh p-SiO (inset: SAED). TEM image of p-SiO after d) 1 cycle, e) 10 cycles, and f) 50 cycles (inset: SAED). g) Correlation between Si domain size/crystallinity and electrochemical stability compiled from literature.

1. Si domain size and density: The Si nanodomains should be as small and dense as possible. Coarsened Si nanodomains are electrochemically unfavorable, as they reduce activity and promote the formation of the $Li_{15}Si_4$ phase, leading to severe volume expansion and particle fracture.[25] Sub-3 nm Si suppresses the formation of unstable $Li_{15}Si_4$ and minimizes structural failure risk.[10]
2. Crystallinity of Si: The crystallinity of Si should be maximized to enhance the electrochemical kinetics. Higher crystallinity promotes faster ion diffusion, reduces polarization, and improves cycling stability, helping to maintain structural integrity under strain.[28]
3. Crystallinity of SiO_2: The crystallinity of SiO_2 must be carefully controlled to prevent excessive rigidity, which reduces its buffering ability for volume expansion, hinders Li^+ transport, and impairs the interfacial kinetics.[29−31] A moderately amorphous SiO_2 matrix offers better mechanical flexibility and facilitates faster Li^+ diffusion.

However, conventional tube-furnace heating involves prolonged heating and cooling processes, resulting in poor thermal control and low heat-transfer efficiency. The excessive thermal budget promotes Si growth and coalescence and may also induce overcrystallization of the SiO_2 matrix.[23−25] Therefore, simultaneously regulating Si nanodomain size, Si crystallinity, and SiO_2 matrix crystallization remains a major challenge. To overcome these limitations, we employ pulsed flash Joule heating (FJH) to induce controlled thermal disproportionation of SiO. The ultrafast heating and cooling process enables rapid, nonequilibrium structural reconstruction, allowing small Si nanodomains to form while suppressing excessive Si coarsening and SiO_2 crystallization. Recently, FJH has emerged as an effective strategy for structural engineering of Si-based anodes. Pan et al. used FJH to generate uniformly dispersed 2−5 nm SiC dispersoids within Si-based alloys, thereby improving structural stability and interfacial integrity.[32] Wang et al. applied rapid Joule heating to construct shell−shell Si/C structures capable of accommodating volume variation during cycling.[33] These studies demonstrate the capability of FJH to direct rapid phase reactions and structural reconstruction in Si-based anodes. Nevertheless, its use for regulating the disproportionation behavior of SiO and prestabilizing sub-2 nm Si nanodomains within an amorphous SiO_2 matrix remains largely unexplored.

In this work, we show that three 0.1 s FJH pulses, rather than a single 0.3 s pulse, generate a higher density of ∼1.5 nm Si nanodomains with improved crystallinity while maintaining a predominantly amorphous SiO_2 matrix. LiOH is introduced as a transient mediator to enhance heat transfer and promote Si nanodomain crystallization during the ultrafast thermal process. The resulting well-mixed Si/SiO_2 dual-phase architecture forms a bulk-stabilized composite, in which dense ultrafine Si nanodomains reduce local stress, suppress volume expansion, and facilitate charge transfer. In addition, single-walled carbon nanotubes (SWCNTs) are incorporated to reinforce the electrode-level conductive network and mechanical integrity. As a result, the optimized FJH-SiO anode delivers a reversible capacity of 1419 mAh g^{-1} with 96.6% retention after 150 cycles, limited electrode swelling of 21.8%, and robust full-cell performance with 88.6% retention after 300 cycles. This work establishes nanodomain prestabilization as a key design principle for SiO-based anodes and provides an energy-efficient route for controlled structural evolution, with nearly 3 orders of magnitude lower energy consumption than conventional annealing.

https://doi.org/10.1021/jacs.6c04827
J. Am. Chem. Soc. 2026, 148, 26017−26026

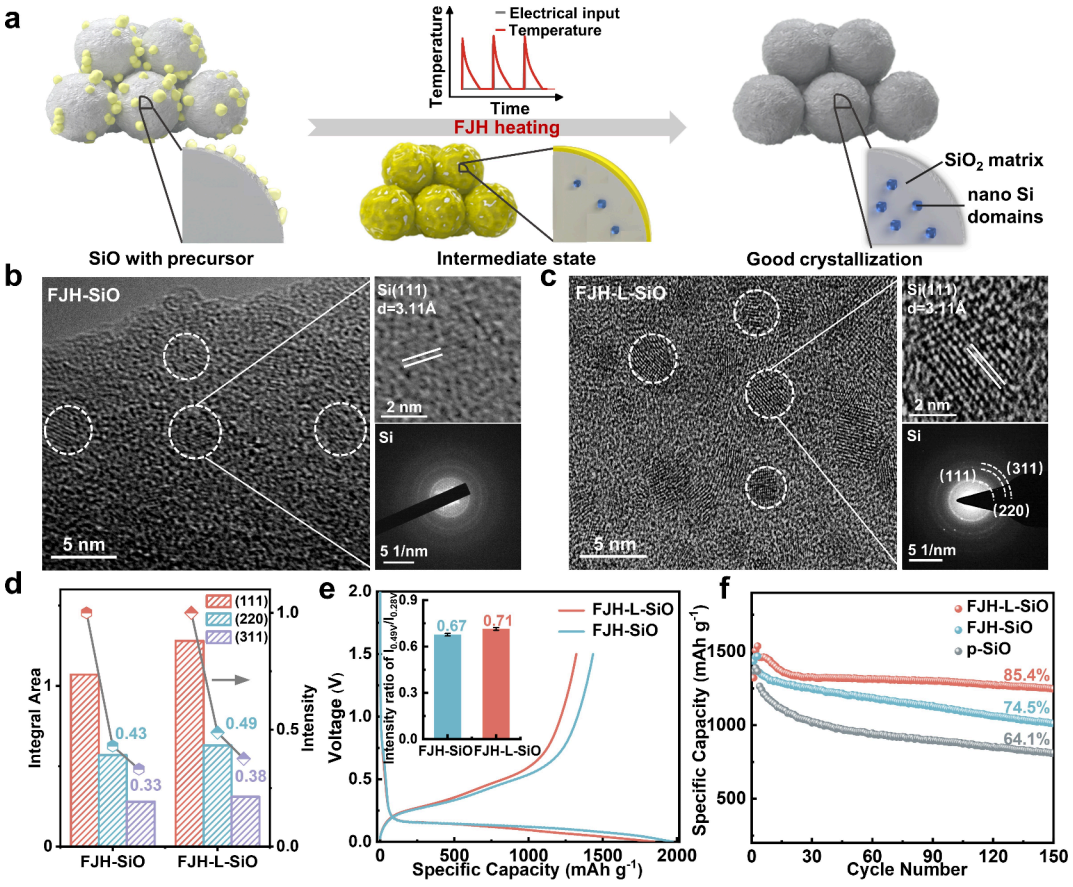

Figure 2. Role of LiOH in promoting crystallization during FJH-induced disproportionation of SiO. a) Schematic illustration of LiOH-assisted FJH disproportionation. b–c) TEM images, corresponding HRTEM, and SAED patterns of FJH-SiO and FJH-L-SiO, respectively. d) Semiquantitative crystallinity analysis based on the integrated area ratio of crystalline Si diffraction peaks to total scattering intensity and relative peak intensity normalized to the Si (111) reflection. e) First charge–discharge profiles (inset: Crystallinity index $I_{0.49\ V}/I_{0.28\ V}$ derived from dQ/dV plots). f) Cycling performance of p-SiO, FJH-SiO, and FJH-L-SiO half-cells.

RESULTS AND DISCUSSION

Electrochemical Disproportionation-Induced Si Nanodomains in SiO

Meta-analysis of literature data reveals a universal trend in SiO electrodes: two-stage capacity fading behavior. Typically, a rapid capacity decay occurs during the initial cycles (attenuation rate K1), followed by a much slower decline (K2, with K1 > K2) (Figure 1a,b).This indicates that the electrochemical stability of SiO is not constant but gradually improves with the cycling. The steep early capacity decay followed by stabilization can be observed in galvanostatic and dQ/dV profiles (Figure S1). Pristine SiO suffers from severe early capacity loss but progressively approaches a metastable, stabilized state after sufficient activation.

The structural evolution of SiO during cycling was further studied. Fresh pristine SiO (p-SiO) exhibits a uniform amorphous structure with no detectable crystalline domains (Figure 1c). After the first cycle, isolated Si nanodomains emerge within the amorphous matrix, marking the onset of phase separation (Figure 1d). By the 10th cycle, these domains enlarge but remain heterogeneous (Figure 1e). During this rapid fading stage (K1), cleavage of Si–O bonds releases metastable Si atoms, which nucleate into small, poorly crystallized domains distributed unevenly across the matrix. After 50 cycles, the density of Si nanodomains increased, with an average diameter of ∼3.2 nm, embedded throughout the matrix (Figure 1f and S2). Weak SAED rings suggest limited crystallinity of the Si nanodomains. With continued cycling, atomic diffusion and interfacial reorganization drive domain redistribution: unstable small domains dissolve, while stable ones grow and homogenize.

We define this structural evolution as the electrochemical disproportionation of SiO, which can be described by the following reaction:

$$2\mathrm{SiO} + (4 - 2y + x)\mathrm{Li}^{+} + (4 - 2y + x)\mathrm{e}^{-} \rightarrow (2 - y)\mathrm{Li}_2\mathrm{O} + \mathrm{Li}_x\mathrm{SiO}_y + \mathrm{Si} \quad (2)$$

During lithiation, the redox cleavage of Si–O bonds reduces part of SiO to elemental Si, while the remainder forms lithium silicates (e.g., Li_4SiO_4 and Li_2SiO_3) and Li_2O,[34] which can improve ionic transport.[35] These observations highlight that the formation of Si nanodomains is critical to stabilizing SiO electrodes. This conclusion is also supported by thermal disproportionation studies, which show that SiO bulk phase can generate Si nanoparticles that enhance electrochemical performance.[25]

Statistical analysis of literature data on Si nanodomain size, crystallinity, and electrochemical performance (specific capacity and capacity retention) highlights the critical influence of domain characteristics (Figure 1g). The degree of crystallization, inferred from the intensity ratio between the 0.49 and 0.28 V peaks,[28] increases with domain size. However,

https://doi.org/10.1021/jacs.6c04827
J. Am. Chem. Soc. 2026, 148, 26017–26026

the relationship between capacity, retention, and Si domain size follows a nonmonotonic "volcano-type" trend rather than a linear one. Electrodes containing excessively small, poorly crystallized Si nanodomains or overly large, highly crystallized ones exhibit rapid capacity fading, whereas domains that balance size and crystallinity deliver higher reversible capacity and cycling stability. When domains exceed a critical size, they undergo two-phase lithiation to form $Li_{15}Si_4$, resulting in substantial volume expansion and accelerated capacity decay.[23] This analysis reveals that electrochemical performance is governed not by size alone but by the combined effects of domain size, crystallinity, and density—underscoring the importance of balanced structural regulation for optimal performance. In contrast, conventional thermal treatments with slow heating and cooling rates typically produce Si nanodomains larger than 3 nm with poorly controlled crystallinity, which ultimately degrades long-term cycling stability.

Structure Engineering of SiO via FJH Disproportionation

Controlling Si nanodomains through electrochemical or conventional thermal disproportionation remains challenging. Flash Joule heating (FJH), with rapid heating and cooling rates exceeding 10^4 °C s^{-1}, enables precise regulation of Si nanodomain formation through rapid, nonequilibrium heating and cooling. A schematic of the FJH disproportionation process is shown in Figure 2a. This ultrafast process generates sub-2 nm Si domains while suppressing SiO_2 crystallization (denoted as FJH-SiO). To further limit nanodomain growth, three 0.1 s pulses were applied instead of a single 0.3 s pulse. In addition, previous studies suggest that LiOH enhances heat transfer efficiency; once the local temperature exceeds its melting point (~465 °C), it forms a transient liquid phase that uniformly wets the particle surface, creating a solid−liquid interfacial layer that facilitates atomic transport.[36] Moreover, Li^+ acts as a network modifier, weakening Si−O bonds and lowering the energy barrier for bond cleavage and structural rearrangement.[37] Previous NaOH-assisted SiO disproportionation under conventional thermal annealing has shown that NaOH can promote Si−O bond rearrangement and accelerate the formation of crystalline Si within the SiO_x matrix. However, the prolonged annealing process also facilitates oxygen migration and SiO_2 crystallization, leading to the formation of a crystalline SiO_2 shell, such as cristobalite.[38] In contrast, the present LiOH-assisted FJH treatment proceeds under an ultrafast, nonequilibrium time−temperature profile, which promotes rapid Si−O rearrangement while suppressing extensive phase separation, Si-domain coarsening, and SiO_2 crystallization. Consequently, LiOH serves as a transient mediator during the FJH process, promoting the formation of well-crystallized Si nanodomains confined within an amorphous SiO_x/SiO_2 matrix (modified SiO is denoted as FJH-L-SiO).

SEM images (Figure S3) indicate that the overall morphology of SiO remains well-preserved after FJH treatment. TEM analysis (Figure 2b) further confirmed the formation of Si nanodomains within the bulk material. Without LiOH, the nanodomains are sparsely distributed, and the corresponding SAED pattern exhibits only diffuse halos, indicating limited crystallinity. In contrast, with 5 wt % LiOH assistance, a dense population of ultrasmall Si nanocrystals with distinct lattice fringes appears within the amorphous matrix (Figure 2c). The corresponding SAED rings are sharp and well-defined, confirming that LiOH effectively promotes nanodomain crystallization. TEM observations of samples with different LiOH contents show that the Si nanodomain size remains largely unchanged, while differences in the crystallinity and spatial uniformity become apparent. The most well-defined and homogeneous Si nanodomains are observed at 5 wt % LiOH (Figure S4).

XRD patterns in Figure S5 reveal the emergence of distinct Si diffraction peaks after FJH treatment, confirming the occurrence of disproportionation. Three characteristic reflections at 2θ = 28.4°, 47.3°, and 56.1° can be assigned to the (111), (220), and (311) planes of crystalline Si, respectively (PDF#27−1402). The FJH-L-SiO sample displays similar diffraction features but exhibits slightly stronger Si peaks compared with FJH-SiO. Semiquantitative analysis of the integrated areas and relative intensities of the Si diffraction peaks (Figure 2d) shows that the simultaneous enhancement of all three peaks in FJH-L-SiO provides direct evidence of reduced lattice defect density and an overall higher degree of Si crystallinity.

Electrochemical measurements were further conducted to evaluate the influence of LiOH on the battery performance. The first-cycle voltage profiles and corresponding differential capacity (dQ/dV) curves of each sample (Figure 2e and S6) show typical lithiation/delithiation features of SiO-based anodes. Quantitative dQ/dV analysis reveals that the intensity ratio between the delithiation peaks at 0.49 V ($Li_{2.0}Si \rightarrow Si$, Region II) and 0.28 V ($Li_{3.5}Si \rightarrow Li_{2.0}Si$, Region I)[39] increases from 0.67 ± 0.08 to 0.71 ± 0.09 upon LiOH addition, indicating the formation of more crystalline Si domains that promote the higher-potential phase transition. X-ray photoelectron spectroscopy (XPS) and electrochemical impedance spectroscopy (EIS) after the first cycle (Figure S7 and S8) show largely similar SEI compositions and interfacial impedance across these samples, with only a slight increase in inorganic components for the LiOH-assisted sample. These results suggest that LiOH has a limited influence on interfacial chemistry, and the minor ICE difference is mainly associated with subtle variations in structural evolution and initial polarization.

The long-term cycling stability of the electrodes prepared with different LiOH contents is shown in Figure 2f and Figure S9. Among them, the FJH-5L-SiO sample exhibits the most stable cycling behavior, maintaining a reversible capacity of 1247 mAh g^{-1} after 150 cycles with a capacity retention of 85.4%, which is 21.3% higher than that of p-SiO and 10.9% higher than that of FJH-SiO. These results indicate that the FJH process significantly enhances both capacity and stability by preforming Si nanodomains within the SiO_2 matrix, while the addition of LiOH further amplifies this effect by promoting higher crystallinity and improved structural uniformity of the Si domains. The energy consumption of the FJH disproportionation process is estimated to be only 2.23 Wh g^{-1}, more than 3 orders of magnitude lower than that of conventional annealing (~3 kWh g^{-1}, Figure S10), highlighting its exceptional energy efficiency.

Optimization of the FJH Thermal Parameters

To regulate the disproportionation process, LiOH-assisted FJH treatments were performed at different target temperatures of 1000, 1100, 1200, and 1600 °C while keeping the pulse scheme fixed at three consecutive 0.1 s pulses. The TEM images in Figure 3a, b, c, and d show that both the morphology

https://doi.org/10.1021/jacs.6c04827
J. Am. Chem. Soc. 2026, 148, 26017−26026

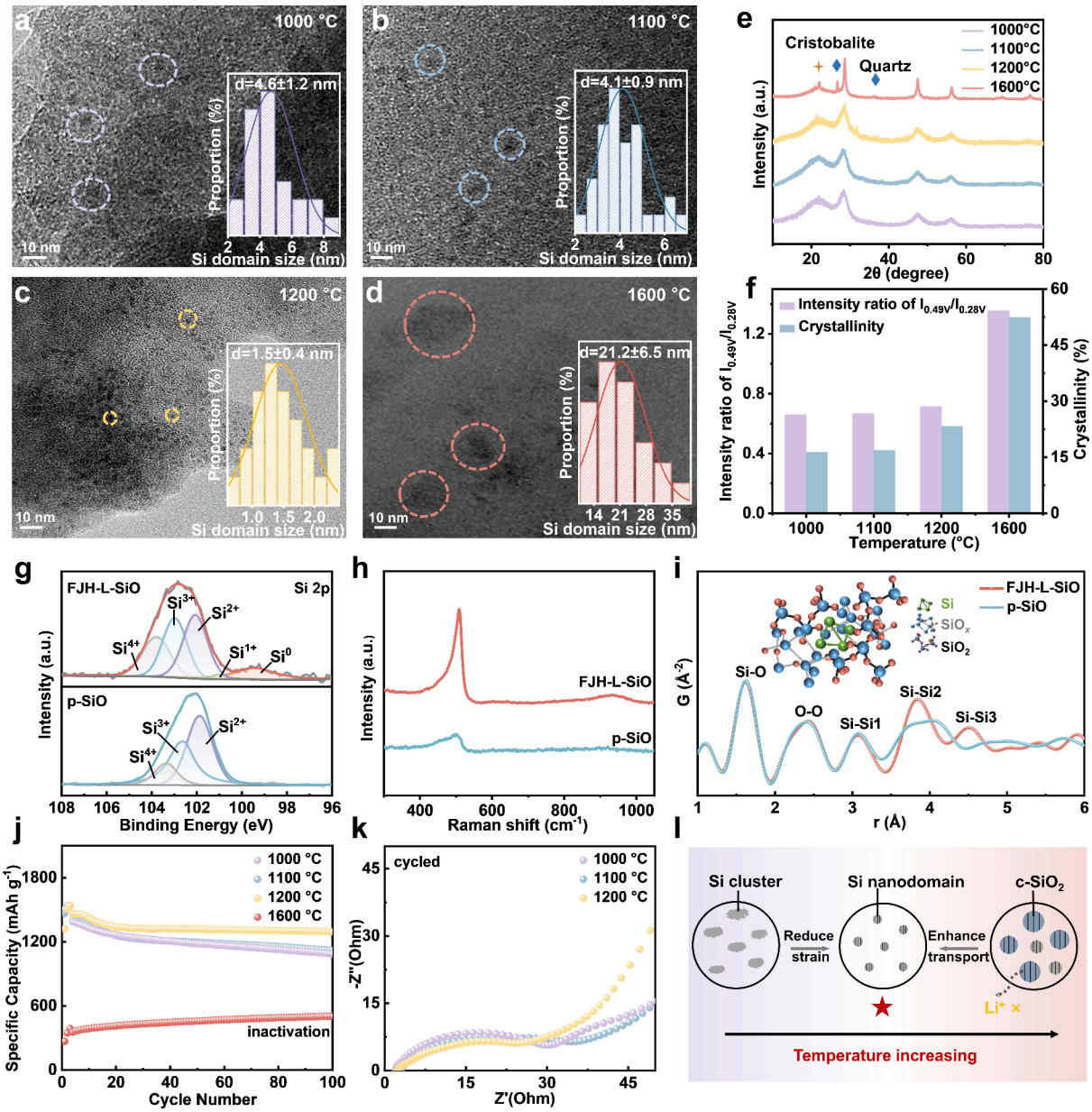

Figure 3. Temperature-dependent morphology evolution and structural characterization of FJH-L-SiO. a-d) Representative TEM images and corresponding size distribution of four samples at different FJH temperatures: a) 1000 °C, b) 1100 °C, c) 1200 °C, and d) 1600 °C. e) XRD patterns of the samples treated at different temperatures. f) Crystallinity evolution with temperature derived from XRD using the integrated peak area method, together with the electrochemical descriptor $I_{0.49\ V}/I_{0.28\ V}$. g) XPS elemental maps of SiO before (blue) and after (red) FJH treatment. h) Raman spectra of SiO. (i) PDF profiles of SiO. j) Cycling performance of LiOH-assisted FJH-treated SiO samples prepared at different target temperatures. k) EIS after three cycles at 0.1C. l) A schematic illustration of the microstructure evolution as a function of FJH temperature.

and size distribution of Si nanodomains vary markedly with the applied temperature. At 1000 °C, partially crystallized Si domains with an average diameter of ∼4.6 nm are embedded within an amorphous matrix. Increasing the temperature to 1100 °C yields slightly smaller and more uniformly dispersed nanocrystals (∼4.1 nm). At 1200 °C, numerous uniformly distributed nanodomains with sizes of ∼1.5 nm emerge, indicating that disproportionation is fully activated while grain coarsening remains effectively suppressed. However, further elevating the temperature to 1600 °C leads to the formation of large ∼21 nm crystalline domains, suggesting excessive atomic diffusion and coalescence. The unexpectedly large Si domains observed at lower temperatures arise from the nonequilibrium nature of FJH,[40] where incomplete Si−O bond cleavage produces aggregated, poorly crystallized Si clusters. At higher temperatures, complete disproportionation generates abundant small Si nuclei. Consequently, the final grain size is governed by the competition between nucleation and coarsening, rather than by temperature alone.

XRD patterns confirm the formation of crystalline Si in all samples after FJH treatment (Figure 3e). The sample treated at 1600 °C exhibits highly intense and sharp Si diffraction peaks, accompanied by additional reflections corresponding to quartz-type SiO_2 and cristobalite. The appearance of these phases indicates that the originally amorphous SiO_2 matrix has undergone substantial overcrystallization. Semiquantitative analysis based on the integrated peak areas (Figure 3f) reveals a clear increase in Si crystallinity with rising temperature, with

https://doi.org/10.1021/jacs.6c04827
J. Am. Chem. Soc. 2026, 148, 26017−26026

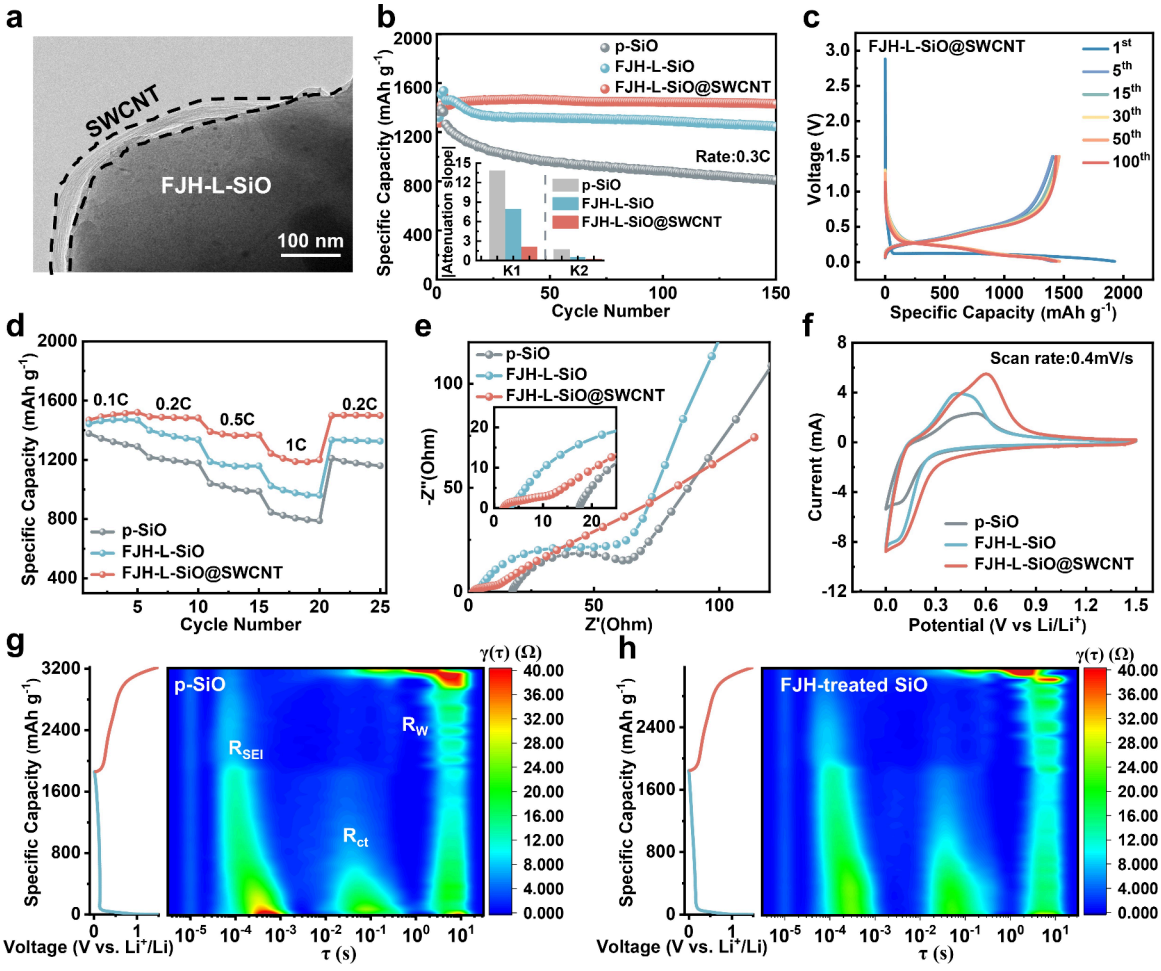

Figure 4. Electrochemical performance comparison of p-SiO, FJH-L-SiO, and FJH-L-SiO@SWCNT electrodes. a) TEM image of FJH-L-SiO@SWCNT. b) Rate performance of p-SiO, FJH-L-SiO, and FJH-L-SiO@SWCNT electrodes (inset: extracted fading rates (K1, K2) from cycling performances). c) Galvanostatic charge−discharge profiles of FJH-L-SiO@SWCNT anodes. d) Rate performance of the three electrodes. e) EIS of the three electrodes. f) CV curves of the three electrodes at the first cycle with a scan rate of 0.4 mV s^{-1}. g) DRT spectrum of the p-SiO electrode. h) DRT spectrum after the FJH treatment.

the 1600 °C sample reaching the highest value of approximately 52.4%. This trend is further supported by dQ/dV analysis of the first delithiation process: the $I_{0.49\ V}/I_{0.28\ V}$ ratio increases to 1.35 at 1600 °C, corroborating the markedly enhanced Si crystallinity at this temperature.

However, as shown in Figure S11, the 1600 °C sample exhibits negligible electrochemical activity, which can be attributed to the high crystallinity of SiO_2, an electrochemically inert phase that impedes lithium-ion transport, as well as the excessive coarsening of Si grains, which reduces their electrochemical reactivity.[30,31] These findings highlight 1200 °C as the optimal temperature, where disproportionation and crystal growth reach a balanced equilibrium, resulting in compact nanodomains with well-controlled crystallinity and confinement. This demonstrates that the size and crystallinity of Si domains can be effectively tuned by adjusting the FJH treatment conditions.

The optimized 1200 °C sample was further analyzed using XPS and high-resolution Si 2p spectra (Figure 3g). These analyses reveal that p-SiO is primarily characterized by Si^{2+} (101.9 eV), while FJH-L-SiO exhibits new peaks corresponding to Si^0 (99.4 eV) and Si^{1+} (100.9 eV), along with an increased Si^{4+} component (103.5 eV). These changes are consistent with the disproportionation of SiO and the formation of Si embedded in a SiO_2 matrix. Raman spectra (Figure 3h) exhibit a sharp crystalline Si peak at 509 cm^{-1} after FJH treatment, accompanied by a blue shift and the emergence of the second-order optical phonons of c-Si at 930 cm^{-1},[41] confirming the increased Si crystallinity in SiO samples.

The local structure of FJH-disproportionated SiO at 1200 °C was further analyzed using atomic pair distribution function (PDF) analysis (Figure 3i), which reveals peaks at 1.6 Å, 2.3 Å, 3.1 Å, 3.8 Å, and 4.5 Å, corresponding to Si−O and O−O bonds in SiO_4 tetrahedra as well as Si−Si1, Si−Si2, and Si−Si3 distances in crystalline silicon.[29] The coordination environment of SiO_4 tetrahedra and the nearest Si−Si pairs are consistent in both samples. Notably, the appearance of Si−Si2 and Si−Si3 correlations after FJH treatment confirms the development of medium-range atomic ordering within the silicon phase. Crystalline Si and SiO_2 models were used to fit the PDF data, resulting in a reasonable fit quality that validates the short-range local structure (Figure S12). The residual fitting deviations are attributed to interfacial silicon suboxides (SiO_x, $0 < x < 2$), as suggested by previous studies.[42] These results collectively demonstrate that FJH-L-SiO forms a composite with crystalline Si domains embedded in an amorphous SiO_2 matrix, interconnected by mixed-valence SiO_x interfaces (inset of Figure 3i).

https://doi.org/10.1021/jacs.6c04827
J. Am. Chem. Soc. 2026, 148, 26017−26026

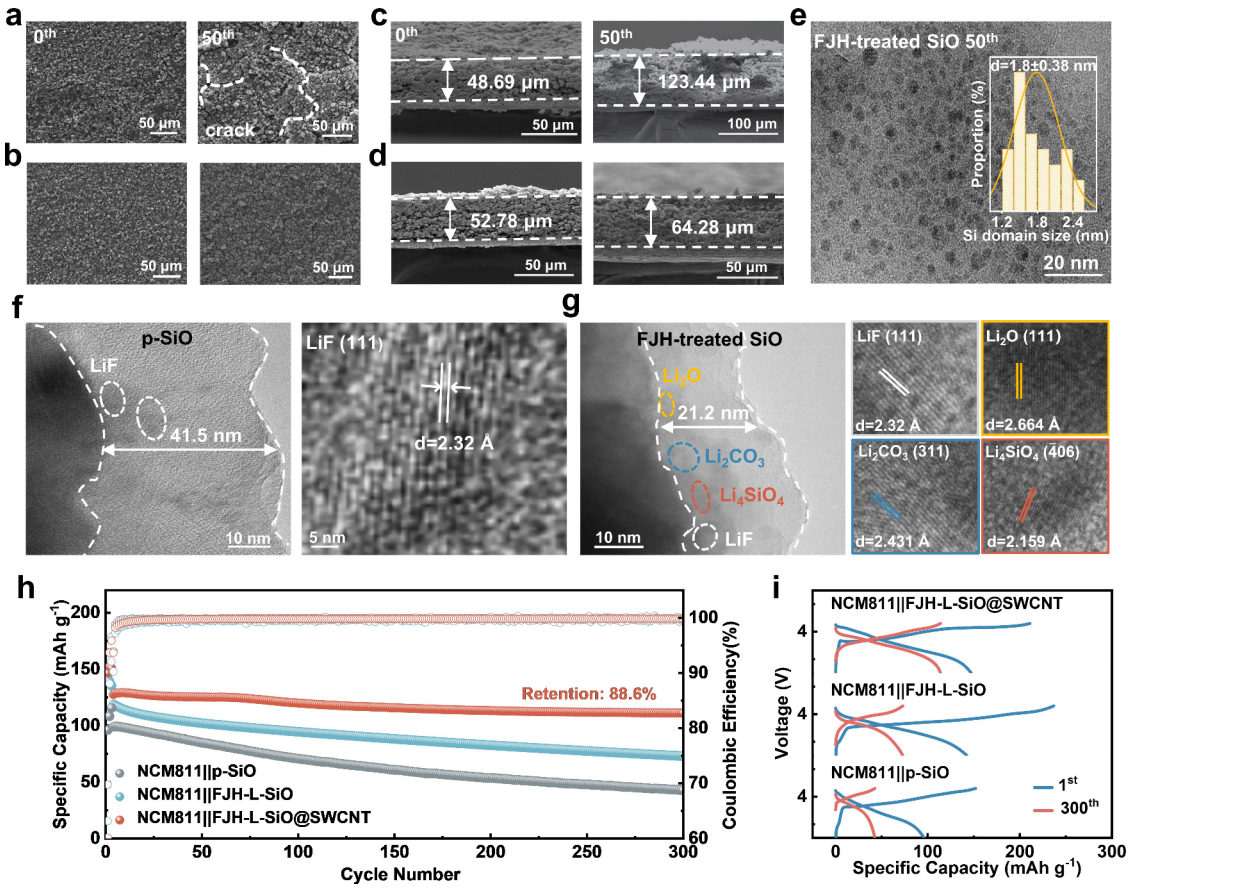

Figure 5. Postcycling analysis of FJH-treated SiO. Top-viewed SEM images of a) p-SiO and b) FJH-treated SiO electrodes before and after 50 cycles. c) Cross-sectional SEM images of p-SiO electrodes before cycling and after 50 cycles, respectively. d) Cross-sectional SEM images of FJH-treated SiO electrodes before cycling and after 50 cycles, respectively. e) TEM image of FJH-treated SiO after 50 cycles (inset: size distribution). f) Cryo-TEM image of p-SiO electrode after 50 cycles. g) Cryo-TEM image of the FJH-treated SiO electrode after 50 cycles. h) Long-term cycling stability of p-SiO, FJH-L-SiO, and FJH-L-SiO@SWCNT electrodes at 0.5C and average Coulombic efficiencies of the three electrodes. (i) Galvanostatic charge−discharge profiles of NCM811 full cells with three anodes.

The electrochemical performance of the SiO samples treated at different temperatures was further tested. As shown in Figure 3j, the 1200 °C electrode demonstrates the highest cycle capacity of 1294.9 mAh g^{-1} and maintains 88.6% capacity retention after 100 cycles. The 1200 °C electrode also delivers an outstanding rate capability of 767.5 mAh g^{-1} at 2 C, which is 26.6% and 21.5% higher than that of the 1000 and 1100 °C electrodes, respectively (Figure S13). EIS reveals that the 1200 °C sample exhibits the lowest charge-transfer resistance (Figure 3k), indicating the formation of a highly conductive interface. Galvanostatic intermittent titration (GITT) profiles (Figure S14) show enhanced Li^+ diffusion coefficients, suggesting that the finely dispersed, crystalline nanodomains facilitate efficient ion transport. As summarized schematically in Figure 3l, the optimized 1200 °C condition yields a Si/SiO_2 nanocomposite with dense ∼1.5 nm crystalline domains that effectively buffer volume expansion, reduce interfacial resistance, and maintain long-term cycling stability.

Electrochemical Performance and Postcycling Analysis of FJH-Treated SiO

To further enhance interfacial contact and improve the electrochemical performance of FJH-treated SiO, a 1 wt % single-walled carbon nanotube (SWCNT) suspension was introduced during the FJH process. SEM and TEM images in Figure S15 and Figure 4a reveal that SWCNTs can uniformly wrap the surface of the SiO particles, forming a conductive network. Moreover, the sub-2 nm Si nanodomains remain intact after SWCNT incorporation (Figure S16), indicating that the addition of SWCNTs during FJH does not affect the predefined nanodomain architecture of FJH-L-SiO. In addition, XRD, Raman, and XPS analyses (Figure S17) show no detectable SiC-related signals after SWCNT incorporation, indicating that the SWCNTs remain largely intact without observable interfacial reaction with the SiO matrix under the present FJH conditions.

The cycling performances of p-SiO and FJH-treated SiO with and without SWCNTs are shown in Figure 4b. Compared with p-SiO, the FJH-L-SiO electrode exhibits markedly reduced fading rates, with the attenuation slope K1 decreasing from 13.8 to 7.9. After 150 cycles at 0.3C, the capacity retention of FJH-L-SiO reaches 85.4%, far exceeding the 58.3% retention of p-SiO, demonstrating that prestabilization effectively suppresses the capacity fading. Notably, the residual early stage decay mainly arises from irreversible lithium consumption and SEI formation in SiO, although it is significantly mitigated compared with p-SiO. Upon SWCNT incorporation during the FJH process, K1 further decreases to 1.1 while K2 remains as low as 0.2, indicating that both early stage and long-term fading are improved. This behavior is associated with the formation of an integrated conductive network intimately coupled with the SiO matrix during FJH.

https://doi.org/10.1021/jacs.6c04827
J. Am. Chem. Soc. 2026, 148, 26017−26026

FJH-L-SiO@SWCNT anode shows good long-term stability, with a high initial capacity of 1419 mAh g^{-1} and retains 96.6% of its capacity after 150 cycles at 0.3C. The corresponding charge−discharge profiles (Figure 4c and S18) reveal substantially reduced polarization and highly stable voltage plateaus throughout cycling. In addition, the dQ/dV plot of p-SiO decays rapidly with cycling, indicating active-site loss and parasitic phase formation (Figure S19). By contrast, FJH-L-SiO@SWCNT retains nearly identical profiles during cycles without $Li_{15}Si_4$ signals (characteristic peak at 450 mV), implying a stable single-phase lithiation mechanism governed by a structurally preserved framework. These results highlight the synergistic contributions of bulk structural stabilization and SWCNT-enabled interfacial/electrode reinforcement in achieving durable cycling performance.

Figure 4d displays the rate performance of p-SiO and FJH-treated SiO with and without SWCNTs. It is evident that the rate performance is significantly improved after FJH treatment and is further enhanced with the incorporation of SWCNTs. The improved rate capability arises from the synergistic combination of bulk stabilization—provided by dense, crystalline Si nanodomains—and the enhanced interfacial conductivity imparted by the SWCNT network. EIS (Figure 4e) shows that the addition of SWCNTs decreases the charge-transfer resistance, indicating accelerated interfacial charge-transport kinetics enabled by continuous conductive pathways bridging individual particles. As shown in Figure S20, GITT analysis and the calculated D_{Li^+} of FJH-L-SiO@SWCNT electrode for the delithiation process is always higher than that of the FJH-L-SiO and p-SiO electrode, because SWCNTs act as the lithium-ion diffusion channel and promote the transport kinetics of the lithium ion between the electrode and the electrolyte. Furthermore, cyclic voltammetry (CV) (Figures 4f and S21) reveals stronger current responses, larger integrated areas, and a positively shifted anodic peak for FJH-L-SiO@SWCNT compared with FJH-L-SiO, confirming reduced polarization and faster lithiation/delithiation processes.

Figure 4g,h shows the distribution of relaxation times (DRT) analysis before and after FJH treatment. Three characteristic processes: interfacial impedance R_{SEI} (10^{-3}–10^{-4} s), charge transfer impedance R_{ct} (1–10^{-2} s), and diffusion impedance R_w (1–10 s), respectively. Compared with p-SiO, FJH-treated SiO exhibits reduced R_{SEI} and R_w, indicating facilitated Li^+ transport across the SEI and within the solid phase. A moderate increase in R_{ct} is observed after FJH, likely due to the higher SiO_2 fraction generated during disproportionation (as confirmed in Figure 3g).

The structural integrity of the electrodes after cycling was further evaluated. As shown in Figure 5a, the p-SiO electrode undergoes severe cracking and delamination after 50 cycles, with its thickness increasing from 48.7 to 123.4 μm—a 153.5% volumetric expansion (Figure 5c). In contrast, the FJH-treated SiO electrode exhibits only minor surface collapse (Figure 5b) and a modest 21.8% thickness increase from 52.8 to 64.3 μm (Figure 5d). Compared with the TEM images of p-SiO after 50 cycles (Figure 1f and S2), which shows larger and heterogeneously distributed Si nanodomains with noticeable aggregation, the Si nanodomains after FJH treatment retain their size and dispersion throughout cycling (Figure 5e and S22), coarsening only slightly to ∼1.8 nm without any indication of aggregation after 50 cycles. The presence of these ultrasmall, uniformly distributed Si nanodomains after FJH treatment effectively suppresses the formation of large, asynchronous Si agglomerates and ensures a more homogeneous stress distribution within the electrode, thereby preventing crack initiation and propagation during repeated lithiation.

Cryo-transmission electron microscopy (cryo-TEM) was further performed to examine the evolution of the SEI during cycling. After 50 cycles, the p-SiO electrode develops a thick (∼41.5 nm) SEI layer primarily composed of organic species, accompanied by a minor fraction of LiF (Figure 5f), whereas the FJH-treated SiO electrode maintains a much thinner (∼21.2 nm) SEI enriched with inorganic species such as LiF, Li_2O, Li_2CO_3, and Li_4SiO_4 (Figure 5g). The chemical composition of the SEI was further examined by XPS depth profiling (Figure S23). Compared with p-SiO, the FJH-treated SiO electrode exhibits a stronger LiF signal in the F 1s spectra and reduced contributions from organic species, such as C−O and C=O, in the C 1s spectra, indicating a higher fraction of inorganic components. Moreover, the inorganic species remain relatively stable with increasing sputtering time, suggesting the formation of a more uniform and inorganic-rich SEI structure. Such thinner, inorganic-rich SEI layers are generally associated with lower electrolyte consumption and enhanced mechanical robustness, as inorganic components are denser and less reactive.[43] The suppressed SEI growth on FJH-treated SiO is consistent with the earlier structural observations, confirming that the improved cycling stability effectively mitigates excessive SEI thickening.

We further investigated the electrochemical performance of the SiO-based anodes paired with NCM811 cathodes in full-cell configurations, with the NCM811 cathode delivering an areal capacity of 2.3 mAh cm^{-2}. As shown in Figure 5h, the NCM811||FJH-L-SiO@SWCNT full cell achieves 88.6% capacity retention after 300 cycles, far surpassing the 51.2% retention of the SWCNT-free counterpart. The average Coulombic efficiency also increases from 98.68% to 99.88%, reflecting improved reversibility and suppressed parasitic reactions. The corresponding charge−discharge curves (Figure 5i) exhibit minimal polarization growth and superior rate performance (Figure S24), confirming that the combination of bulk nanodomain stabilization and interfacial reinforcement ensures robust long-term electrochemical stability in full-cell operation.

CONCLUSION

In summary, this work suggests that electrochemically driven disproportionation contributes to the gradual structural stabilization of SiO during cycling, although this process is kinetically sluggish and is difficult to control. By using pulsed FJH, we realize rapid, nonequilibrium disproportionation of SiO and prestabilize it into a bulk nanocomposite composed of dense sub-2 nm Si nanodomains embedded in a strain-adaptive amorphous SiO_2 matrix. The ultrafast thermal pulses promote rapid Si nucleation while suppressing excessive coarsening and SiO_2 crystallization. LiOH further enhances Si nanodomain crystallinity through transient liquid-phase mediation, whereas SWCNT incorporation reinforces electrode-level conductivity and mechanical integrity. As a result, the optimized architecture effectively mitigates stress accumulation, suppresses electrode swelling, and improves charge-transfer kinetics, leading to stable cycling in both half- and full-cell configurations. More broadly, this study establishes nanodomain prestabilization as a key design principle for SiO-based

https://doi.org/10.1021/jacs.6c04827
J. Am. Chem. Soc. 2026, 148, 26017−26026

anodes and demonstrates FJH as an energy-efficient route for controlled thermal disproportionation, providing new insights and a versatile platform for designing durable high-capacity anodes for next-generation lithium-ion batteries.

■ ASSOCIATED CONTENT

Supporting Information

The Supporting Information is available free of charge at https://pubs.acs.org/doi/10.1021/jacs.6c04827.

Experimental section for characterizations, electrochemical measurements, and material synthesis; more details on particle size distribution, electrochemical performance analyses including CV, dQ/dV, and GITT, SEM images, TEM images, PDF profiles, and XRD patterns (PDF)

■ AUTHOR INFORMATION

Corresponding Authors

Chao Wang − *School of Materials Science and Engineering, Tongji University, Shanghai 201804, China*; Email: chaow@tongji.edu.cn

Yunhui Huang − *State Key Laboratory of Material Processing and Die & Mould Technology, School of Materials Science and Engineering, Huazhong University of Science and Technology, Wuhan, Hubei 430074, China*; orcid.org/0000-0003-1687-1938; Email: huangyh@hust.edu.cn

Authors

Jiarui Li − *School of Materials Science and Engineering, Tongji University, Shanghai 201804, China*

Quan Nie − *School of Materials Science and Engineering, Tongji University, Shanghai 201804, China*

Te Kang − *School of Materials Science and Engineering, Tongji University, Shanghai 201804, China*

Ge Qu − *School of Materials Science and Engineering, Tongji University, Shanghai 201804, China*

Fangzhou Yang − *School of Materials Science and Engineering, Tongji University, Shanghai 201804, China*

Wang Wan − *School of Materials Science and Engineering, Tongji University, Shanghai 201804, China*

Long Yang − *School of Materials Science and Engineering, Tongji University, Shanghai 201804, China*; orcid.org/0000-0001-8731-0172

Complete contact information is available at: https://pubs.acs.org/10.1021/jacs.6c04827

Notes

The authors declare no competing financial interest.

■ ACKNOWLEDGMENTS

This work was supported by the National Key Research and Development Program of China (Grant No. 2022YFB3803400), National Natural Science Foundation of China (Grant Nos. 22579129, 52302193), Natural Science Foundation of Shanghai (Grant No. 25ZR1401358), and the Fundamental Research Funds for the Central Universities. The authors thank the support from the synchrotron radiation PDF experiments were performed at BL02B1 of SPring-8 with the approval of Japan Synchrotron Radiation Research Institute (JASRI, Proposal No. 2024A1878).

■ REFERENCES

(1) Magasinski, A.; Dixon, P.; Hertzberg, B.; Kvit, A.; Ayala, J.; Yushin, G. High-performance lithium-ion anodes using a hierarchical bottom-up approach. *Nat. Mater.* **2010**, *9* (4), 353−358.

(2) Li, X.; Gu, M.; Hu, S.; Kennard, R.; Yan, P.; Chen, X.; Wang, C.; Sailor, M. J.; Zhang, J.-G.; Liu, J. Mesoporous silicon sponge as an anti-pulverization structure for high-performance lithium-ion battery anodes. *Nat. Commun.* **2014**, *5*, 4105.

(3) Chan, C. K.; Peng, H.; Liu, G.; McIlwrath, K.; Zhang, X.; Huggins, R. A.; Cui, Y. High-performance lithium battery anodes using silicon nanowires. *Nat. Nanotechnol.* **2008**, *3* (1), 31−35.

(4) Shi, Y.; Wan, J.; Li, J.; Hu, X.; Lang, S.; Shen, Z.; Li, G.; Yan, H.; Jiang, K.; Guo, Y.; et al. Elucidating the interfacial evolution and anisotropic dynamics on silicon anodes in lithium-ion batteries. *Nano Energy* **2019**, *61*, 304−310.

(5) Ke, C.; Liu, F.; Zheng, Z.; Zhang, H.; Cai, M.; Li, M.; Yan, Q.; Chen, H.; Zhang, Q. Boosting lithium storage performance of Si nanoparticles via thin carbon and nitrogen/phosphorus co-doped two-dimensional carbon sheet dual encapsulation. *Rare Met.* **2021**, *40* (6), 1347−1356.

(6) Park, C.-M.; Kim, J.-H.; Kim, H.; Sohn, H.-J. Li-alloy based anode materials for Li secondary batteries. *Chem. Soc. Rev.* **2010**, *39* (8), 3115−3141.

(7) Choi, J. W.; Aurbach, D. Promise and reality of post-lithium-ion batteries with high energy densities. *Nat. Rev. Mater.* **2016**, *1* (4), 16013.

(8) Liu, Z.; Yu, Q.; Zhao, Y.; He, R.; Xu, M.; Feng, S.; Li, S.; Zhou, L.; Mai, L. Silicon oxides: a promising family of anode materials for lithium-ion batteries. *Chem. Soc. Rev.* **2019**, *48* (1), 285−309.

(9) Hu, T.; Hu, Y.; Guo, Y.; Yang, A.; Chen, X.; Wang, X. Biomolecular-derived conformal carbon coating engineering ultra-stable silicon oxide anodes for lithium-ion batteries. *Chem. Eng. J.* **2025**, *519*, 165466.

(10) Kitada, K.; Pecher, O.; Magusin, P. C. M. M.; Groh, M. F.; Weatherup, R. S.; Grey, C. P. Unraveling the reaction mechanisms of SiO anodes for Li-ion batteries by combining in situ ^{7}Li and ex situ ^{7}Li/^{29}Si solid-state NMR spectroscopy. *J. Am. Chem. Soc.* **2019**, *141* (17), 7014−7027.

(11) Pan, K.; Zou, F.; Canova, M.; Zhu, Y.; Kim, J.-H. Systematic electrochemical characterizations of Si and SiO anodes for high-capacity Li-Ion batteries. *J. Power Sources* **2019**, *413*, 20−28.

(12) Zhang, Z.; Chen, W.; Tian, J.; Zhang, K.; de León Albarrán, C. P.; Wu, C.; Shi, Z.; Li, Z.; Pan, J. H. Two-dimensional nitrogen-doped carbon nanosheets-coated porous SiO composites sponges for durable anode materials of high-energy lithium-ion batteries. *Chem. Eng. J.* **2025**, *518*, 164269.

(13) Huang, T.; Yang, Y.; Pu, K.; Zhang, J.; Gao, M.; Pan, H.; Liu, Y. Linking particle size to improved electrochemical performance of SiO anodes for Li-ion batteries. *RSC Adv.* **2017**, *7* (4), 2273−2280.

(14) Yu, B.-C.; Hwa, Y.; Park, C.-M.; Sohn, H.-J. Reaction mechanism and enhancement of cyclability of SiO anodes by surface etching with NaOH for Li-ion batteries. *J. Mater. Chem. A* **2013**, *1* (15), 4820−4825.

(15) Hu, L.; Xia, W.; Tang, R.; Hu, R.; Ouyang, L.; Sun, T.; Wang, H. Excellent cyclic and rate performances of SiO/C/Graphite composites as Li-ion battery anode. *Front. Chem.* **2020**, *8*, 388.

(16) Cui, J.; Cui, Y.; Li, S.; Sun, H.; Wen, Z.; Sun, J. Microsized porous SiO_x@C composites synthesized through aluminothermic reduction from rice husks and used as anode for lithium-ion batteries. *ACS Appl. Mater. Interfaces* **2016**, *8* (44), 30239−30247.

(17) Wang, J.; Zhao, H.; He, J.; Wang, C.; Wang, J. Nano-sized SiO_x/C composite anode for lithium ion batteries. *J. Power Sources* **2011**, *196*, 4811−4815.

(18) Xu, W.; Sun, Z.; Tang, C.; Cheng, Z.; Sun, W.; Du, A.; Zhang, Q.; Wu, M.; Zhang, H. Biomimetics-driven design of micron-sized SiO composites for high-performance lithium-Ion batteries. *Adv. Funct. Mater.* **2025**, *35* (25), 2422743.

(19) Sun, Z.; Zhang, Z.; Zhou, S.; Liu, W.; Liu, J.; Yin, Q.; Pan, J.; Wu, X.; Zhuang, Z.; Peng, D.; et al. Effective binding sufficiently-small

SiO_2 nanoparticles within carbon nanosheets framework enables a high-performing and durable anode for lithium-ion batteries. *J. Materiomics.* **2025**, *11* (5), 101053.
(20) Yu, B.-C.; Hwa, Y.; Kim, J.-H.; Sohn, H.-J. A new approach to synthesis of porous SiO_x anode for Li-ion batteries via chemical etching of Si crystallites. *Electrochim. Acta* **2014**, *117*, 426−430.
(21) Mamiya, M.; Kikuchi, M.; Takei, H. Crystallization of fine silicon particles from silicon monoxide. *J. Cryst. Growth* **2002**, *237*, 1909−1914.
(22) Hwa, Y.; Park, C.-M.; Sohn, H.-J. Modified SiO as a high performance anode for Li-ion batteries. *J. Power Sources* **2013**, *222*, 129−134.
(23) Wang, J.; Wang, X.; Liu, B.; Lu, H.; Chu, G.; Liu, J.; Guo, Y.; Yu, X.; Luo, F.; Ren, Y.; et al. Size effect on the growth and pulverization behavior of Si nanodomains in SiO anode. *Nano Energy* **2020**, *78*, 105101.
(24) Xu, S.; Hou, X.; Wang, D.; Zuin, L.; Zhou, J.; Hou, Y.; Mann, M. Insights into the Effect of Heat Treatment and Carbon Coating on the Electrochemical Behaviors of SiO Anodes for Li-Ion Batteries. *Adv. Energy. Mater.* **2022**, *12* (18), 2200127.
(25) Park, C.-M.; Choi, W.; Hwa, Y.; Kim, J.-H.; Jeong, G.; Sohn, H.-J. Characterizations and electrochemical behaviors of disproportionated SiO and its composite for rechargeable Li-ion batteries. *J. Mater. Chem.* **2010**, *20* (23), 4854−4860.
(26) Li, H.; Li, H.; Yang, Z.; Yang, L.; Gong, J.; Liu, Y.; Wang, G.; Zheng, Z.; Zhong, B.; Song, Y.; et al. SiO_x anode: from fundamental mechanism toward industrial application. *Small* **2021**, *17* (51), 2102641.
(27) Sun, Z.; Yin, Q.; Zhou, S.; Chen, H.; Wen, S.; Yang, H.; Wu, X.; Pan, J.; Han, J.; Yang, H.; et al. High-Performance Silicon Anodes Enabled by Multifunctional Ultrafine Silica Nanoparticle-Embedded Carbon Coatings for Lithium-Ion Batteries. *Adv. Energy. Mater.* **2025**, *15* (23), 2500189.
(28) He, Z.; Xu, Z.; Long, Y.; Zhu, J.; Yang, H.; Chen, K.; Zhou, Q.; Cao, N.; Wang, X.; Wang, J.; et al. LiOH-mediated crystallization regulating strategy enhancing electrochemical performance and structural stability of SiO anodes for lithium-ion batteries. *Nano Res.* **2024**, *17* (9), 8174−8183.
(29) Cao, Y.; Bennett, J. C.; Dunlap, R. A.; Obrovac, M. N. A simple synthesis route for high-capacity SiO_x anode materials with tunable oxygen content for lithium-ion batteries. *Chem. Mater.* **2018**, *30* (21), 7418−7422.
(30) Choi, G.; Kim, M.; Kang, B. A New Design Rule for Developing SiO with High Performance: Controlling Short-Range Ordering of SiO_2 Phase. *Adv. Energy. Mater.* **2023**, *13* (39), 2302362.
(31) Yamamura, H.; Nobuhara, K.; Nakanishi, S.; Iba, H.; Okada, S. Investigation of the irreversible reaction mechanism and the reactive trigger on SiO anode material for lithium-ion battery. *J. Ceram. Soc. Jpn.* **2011**, *119* (1395), 855−860.
(32) Lan, D.; Ou, P.; Pei, S.; Liu, K.; Li, C.; Zhang, M.; Liu, Y.; He, S.; She, L.; Yang, Y.; et al. Flash joule heating driven in-situ dispersoid synthesis: Mechanical-interfacial-conductive coupling mechanisms in silicon-based anodes. *Energy Storage Mater.* **2026**, *86*, 104956.
(33) Liu, S.; Liu, B.; Yu, Z.; Sun, Z.; Liu, M.; Luo, X.; Wang, M.; Gao, Y.; Wang, B. Rapid Release of Silicon by Ultrafast Joule Heating Generates Mechanically Stable Shell−Shell Si/C Anodes with Dominant Inward Deformation. *ACS Nano* **2024**, *18* (26), 17326−17338.
(34) Zhang, S. S. Electrochemical Insights into the Capacity Fade of Micron-Sized Silicon Anodes in Li-Ion Batteries and a Mitigation Strategy. *J. Electrochem. Soc.* **2025**, *172* (10), 100507.
(35) Jung, S. C.; Kim, H.-J.; Kim, J.-H.; Han, Y.-K. Atomic-level understanding toward a high-capacity and high-power silicon oxide (SiO) material. *J. Phys. Chem. C* **2016**, *120* (2), 886−892.
(36) Hwang, M.; Choi, J. H.; Lee, S.; Hwang, J.; Park, S.; Choi, S.; Kim, M.; Lim, H.; Lim, H.; Oh, M.; et al. tudy of induced liquid-phase sintering effect in lithium-ion battery cathode upcycling. *Joule* **2025**, *9* (10), 102103.
(37) Choi, G.; Kim, J.; Kang, B. High initial coulombic efficiency of SiO enabled by controlling SiO_2 matrix crystallization. *ACS Appl.Mater.Interfaces* **2022**, *14* (39), 44261.
(38) Lee, J.; Lee, K.; Cho, J.; Kim, J.; Choi, N.; Park, S. Chemical-Assisted Thermal Disproportionation of Porous Silicon Monoxide into Silicon-Based Multicomponent Systems. *Angew. Chem., Int. Ed.* **2012**, *51* (11), 2767−2771.
(39) Ogata, K.; Salager, E.; Kerr, C. J.; Fraser, A. E.; Ducati, C.; Morris, A. J.; Hofmann, S.; Grey, C. P. Revealing lithium−silicide phase transformations in nano-structured silicon-based lithium ion batteries via in situ NMR spectroscopy. *Nat.Commun.* **2014**, *5*, 3217.
(40) Yao, Y.; Dong, Q.; Brozena, A.; Luo, J.; Miao, J.; Chi, M.; Wang, C.; Kevrekidis, I. G.; Ren, Z. J.; Greeley, J.; et al. High-entropy nanoparticles: Synthesis-structure-property relationships and data-driven discovery. *Science* **2022**, *376* (6589), eabn3103.
(41) Chung, D. J.; Youn, D.; Kim, J. Y.; Jeong, W. J.; Kim, S.; Ma, D.; Lee, T. R.; Kim, S. T.; Kim, H. Topology optimized prelithiated SiO anode materials for lithium-ion batteries. *Small* **2022**, *18* (27), 2202209.
(42) Hirata, A.; Kohara, S.; Asada, T.; Arao, M.; Yogi, C.; Imai, H.; Tan, Y.; Fujita, T.; Chen, M. Atomic-scale disproportionation in amorphous silicon monoxide. *Nat. Commun.* **2016**, *7*, 11591.
(43) Jagger, B.; Pasta, M. Solid electrolyte interphases in lithium metal batteries. *Joule* **2023**, *7* (10), 2228−2244.

https://doi.org/10.1021/jacs.6c04827
J. Am. Chem. Soc. 2026, 148, 26017−26026